Kelvin force-driven coalescence of oil droplets in a paramagnetic aqueous carrier phase

Xueyong Lu [1], Yuheng He [1,2], Kerstin Eckert [1,2] and Zhe Lei [1,2,*]

[1] *Institute of Fluid Dynamics, Helmholtz-Zentrum Dresden-Rossendorf (HZDR), D-01328 Dresden, Germany*

[2] *Institute of Process Engineering and Environmental Technology, Technische Universität Dresden, D-01069 Dresden, Germany*

(Received 29 January 2026; accepted 13 October 2026; published 13 November 2026)

Predicting the timing of droplet coalescence remains a fundamental challenge because the transition from thin-film drainage to interface rupture is not specified by existing models. While the Stokes-Reynolds-Young-Laplace (SRYL) framework accurately describes hydrodynamic film thinning, it lacks a criterion for the onset of rupture in a chemically complex environment under external compression. To bridge this gap, we employ a contactless magnetic Kelvin force-based apparatus to drive precisely controlled, head-on droplet collisions to investigate the drop-drop coalescence behavior. Using this platform, we systematically measure the coalescence residence time under varied material properties. To facilitate the analysis of these results, we present a dimensionless similarity formulation that lumps the dependence of drainage dynamics on viscosity, interfacial tension, droplet size, and the compressive Kelvin force. This formulation collapses the drainage process onto a single dimensionless master curve, where the drainage curve is uniquely determined by a dimensionless time. By projecting the experimentally measured coalescence residence time onto this master drainage curve, we derive the corresponding rupture thickness for various conditions. The resulting scaling relations provide a quantitative description of droplet coalescence and identify a characteristic hydrodynamic length scale governing thin film rupture. These findings establish a robust framework for modeling and evaluating droplet coalescence in complex, surfactant-laden multiphase systems with highly concentrated electrolytes.

DOI: 10.1103/8tjf-ky6v

I. INTRODUCTION

Coalescence is one of the most fundamental and ubiquitous phenomena in nature [1–3]. It refers to the process by which droplets or bubbles, dispersed within a continuous medium, merge into a larger entity. Coalescence appears as a critical step for raindrop formation and cloud evolution [4]. From an industrial perspective, coalescence plays a dual role. On one hand, the stability of emulsions (droplet dispersion) for food and cosmetics [5,6] relies on retarded coalescence to extend shelf time. On the other hand, efficient coalescence, facilitating demulsification, is key to accelerating phase separation processes, such as crude oil dehydration [6] and the separation and purification of rare-earth elements (REEs) in state-of-the-art hydrometallurgy [2,7–9]. Thus, deep understanding of coalescence has been the focus of intensive scientific research for decades [10,11].

*Contact author: z.lei@hzdr.de

Published by the American Physical Society under the terms of the Creative Commons Attribution 4.0 International license. Further distribution of this work must maintain attribution to the author(s) and the published article's title, journal citation, and DOI.

The theoretical study of coalescence traces back to Reynolds' lubrication theory [12]. It correlates the fluid flow of the liquid film that segregates droplets and bubbles with viscous resistance, capillary pressure, and interfacial mobility [13–16]. The drainage process of the thin liquid film is responsible for preventing instantaneous coalescence upon close contact [1,17]. Vrij, building on Scheludko's foundational work [18], connects the drainage process with the inherently stochastic nature of film rupture [19]. He demonstrated that rupture is not triggered at a definite threshold, known as critical film thickness [18,20,21]. Instead, it could be initiated by the growth of thermal capillary waves and destabilized by attractive van der Waals force [20,22]. Practical systems, however, rarely conform to the idealized conditions presumed above. Solvent extraction, for instance, contains surface-active species and typically has high ionic strength [23]. The former diminishes interfacial tension and promotes interface deformation. Both phenomena lead to the dimpled interface at the contact area that hydrodynamically hinders film thinning [11,24,25]. The shear-induced surfactant gradient at the interface generates Marangoni stresses that immobilize tangential surface flow [26,27]. The nonlinear interaction of various viscous, capillary, diffusive, and stochastic timescales renders the prediction of coalescence in such intricate systems highly difficult. Consequently, systematic experimental data for the duration of the coalescence period, known as the coalescence residence time τ_c [6,28–31], acquired under rigorously controlled, and industrially relevant settings are limited. Furthermore, experimental studies for film rupture thickness have largely been conducted on complex and specific configurations [32–37] that do not reflect coalescence in real systems, which is free from a contact with an artificial third phase, such as a solid wall. Indeed, all force- or approaching-velocity-controlled apparatuses used in previous coalescence studies involve either a solid substrate, severe geometric confinement or physical intrusion of capillaries. They are known to deform the droplets, and disturb the delicate drainage flow, which alters the scaling laws of coalescence dynamics [38].

In contrast to all conventional techniques, we introduce a method to quantify τ_c of unbounded droplets that eliminates the need of physical contact with any external object, such as needle or wall. To induce coalescence, our method utilizes Kelvin forces generated by an anti-parallelly magnetized ring-rod permanent magnet assembly [39] to contactlessly drive droplets into head-on collision. In detail, a constant Kelvin force density [40,41], $\boldsymbol{f}_m = \frac{\chi}{2\mu_0} \nabla B^2$ (B—magnetic flux density, μ_0—vacuum permeability, χ—magnetic susceptibility), is imposed onto the droplets, which serves a dual purpose: its vertical component counteracts buoyancy to achieve stable levitation of the organic droplets in a Dy(III) aqueous solution, while its radial component provides a precise compressive force to drive the second droplet towards the first one, initiating coalescence. The entire process, from approach and film drainage to eventual rupture, is monitored optically. We then introduce a dimensionless similarity scheme that describes the drainage process to show that the drainage dynamics collapses onto a unified curve that is independent of fluid properties, droplet size, force, length and time scale. Within this framework, we systematically investigate the dependence of τ_c on a suite of physical parameters, including droplet diameter (ϕ), aqueous bulk viscosity (μ_{aq}), organic droplets viscosity (μ_{oil}), interfacial tension (γ), and the applied normal compressive Kelvin force (F). By projecting the experimentally measured τ_c onto the master drainage curve, we extract the critical rupture thickness h_{coa}. With approximately two thousand valid data points measured, we derive a comprehensive empirical scaling law for τ_c and h_{coa} substantiated by an excellent statistics. Furthermore, by analyzing the statistical distribution of the relative residual of the experimental data with respect to this deterministic law, we seek to quantify the inherent stochasticity of the film rupture process, thereby bridging the gap between macroscopic, deterministic drainage models and the microscopic, random nature of coalescence.

II. MATERIALS AND METHODS

A. Materials and experimental approach

Analytical grade dysprosium(III) oxide (Dy_2O_3, 99.9% Dy, CAS No. 1308-87-8, abcr GmbH) was dissolved in 6.0 M hydrochloric acid (CHEMSOLUTE®) to prepare the aqueous base solutions.

TABLE I. Physical properties of the carrier and dispersed phases, measured at 20 °C.

Composition	ϱ (g/cm^3)	μ (mPa s)	χ (10^{-6})[a,b]
Carrier phase			
Aqueous solutions [c_{Dy} (M)]			
0.8	1.19 ± 0.01	1.8 ± 0.1	464
1.0	1.24 ± 0.01	2.0 ± 0.1	580
1.2	1.28 ± 0.01	2.5 ± 0.1	696
1.5	1.35 ± 0.01	3.0 ± 0.1	870
1.8	1.43 ± 0.01	3.8 ± 0.1	1044
Glycerol mixtures [% v/v in 1.0 M Dy(III)]			
+ 0	1.24 ± 0.01	2.0 ± 0.1	580
+ 8	1.27 ± 0.01	2.9 ± 0.1	580
+ 16	1.29 ± 0.01	4.3 ± 0.2	580
+ 24	1.31 ± 0.01	6.3 ± 0.2	580
+ 32	1.33 ± 0.01	9.4 ± 0.3	580
+ 40	1.36 ± 0.01	13.9 ± 0.5	580
Dispersed phase			
Paraffin oil	0.86 ± 0.01	97 ± 1	
Mineral oil	0.83 ± 0.01	29.9 ± 0.3	
Hexadecane	0.77 ± 0.01	3.5 ± 0.1	−0.64
Heptane	0.68 ± 0.01	0.90 ± 0.04	−0.58
Additive			
Glycerol	1.26 ± 0.01	980 ± 1	−0.78

[a]For diamagnetic organic oils, the molar susceptibility χ_M is related to the volume susceptibility χ by $\chi_M = \chi \cdot (M/\varrho)$.

[b]For the paramagnetic carrier phase, χ is dominated by the Dy(III) ions. The Dy(III) concentration is retained at 1.0 M in all glycerol mixtures, and the minor variations in χ arising from the diamagnetic contribution of glycerol are negligible.

The pH was adjusted to 1.0 using 1 M HCl and characterized using a pH meter (FiveEasy Plus, Mettler-Toledo). The cationic surfactant decyltrimethylammonium bromide (DeTAB, CAS No. 2082-84-0, Sigma-Aldrich) was added to the aqueous phase at concentrations ranging from 0.001 to 1.0 mM to tune the interfacial tension (γ). The viscosity of the aqueous phase (μ_{aq}) was adjusted by adding glycerol (CAS 56-81-5, Sigma-Aldrich) at volume fractions of 0% to 40% (v/v) in 8% increments. Investigation of dispersed phase viscosity was achieved by using various oils, including paraffin oil (CAS 8012-95-1, Supelco), mineral oil (CAS 8042-47-5, Sigma-Aldrich), n-hexadecane (CAS 544-76-3, Alfa Aesar), and n-heptane (CAS 142-82-5, Sigma-Aldrich). All chemicals were used as received. All physical properties were measured at 20 °C. The dynamic viscosity (μ) and density (ϱ) were determined using a Stabinger viscometer (SVM 3001, Anton Paar) with nominal uncertainties of ±0.35% and $\pm 5 \times 10^{-5}$ g cm^{-3}, respectively. Interfacial tensions were measured using a profile analysis tensiometer (PAT-1M, Sinterface Technologies). An overview of the measured material properties is provided in Table I.

The experimental setup is illustrated in Fig. 1(a). The coalescence experiments were conducted in a quartz cuvette (10 × 10 × 40 mm; Hellma GmbH), which provides direct optical access for shadowgraphy measurement. The process was monitored using a high-speed microscope (spatial resolution: 161.5 pixels/mm; frame rates: 50–100 fps). A ring-rod permanent magnet assembly (remanence $B_r = 1.33$ T; grade N45) with anti-parallel magnetization was positioned on top of the cuvette to generate the magnetic gradient.

Organic droplets were generated using a high-precision syringe pump (PHD Ultra, Harvard Apparatus) connected via PTFE tubing and a flow distributor to an angled, blunt-tipped stainless steel

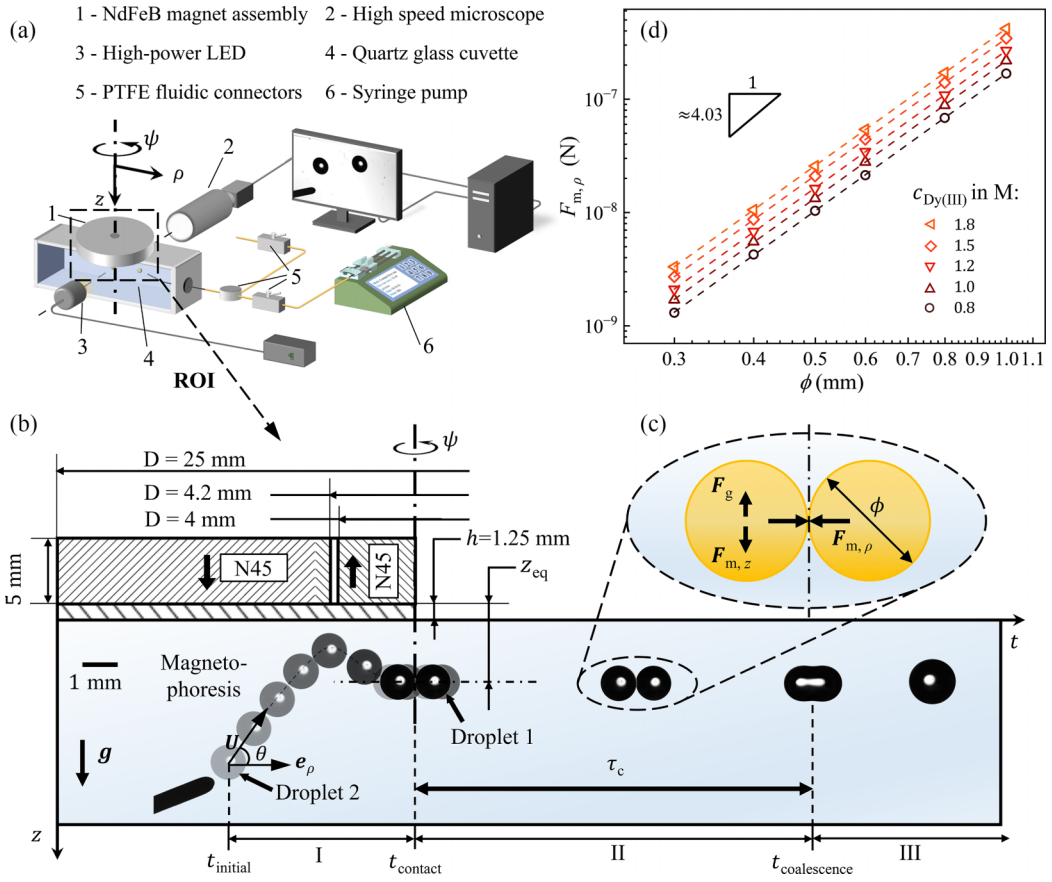


FIG. 1. Experimental system and coalescence process of magnetically manipulated droplets. (a) Schematic of the experimental setup. A cylindrical coordinate system (z, ρ, ψ) is defined, where z, ρ, and ψ denote the vertical direction (aligned with gravity), the radial direction, and the azimuthal angle, respectively. (b) Magnified view of the region of interest (ROI) in (a), highlighting the levitated droplet pair and the optical imaging path. (c) Schematic force diagram showing the Kelvin force ($\boldsymbol{F}_{\mathrm{m}}$) and gravitational force ($\boldsymbol{F}_{\mathrm{g}}$) acting on droplets in equilibrium. (d) Radial component $F_{\mathrm{m},\rho}$ acting as the compressive force for coalescence and its scaling with droplet diameter ϕ in variety of Dy(III) concentrations.

needle (27G; outer diameter 0.41 mm). A microfluidic stopcock was utilized to precisely terminate the fluid injection once the droplet reached the target diameter. In each experiment, the first droplet (Droplet 1) was dispensed at a constant flow rate of 40 μL/min and released into the paramagnetic Dy(III) solution, where it rose until reaching a designated position for magnetic levitation [42]. Droplet 2 was then produced using the identical procedure. Driven by magnetophoresis, Droplet 2 traveled along the trajectory of Droplet 1 until a head-on collision occurred, cf. Fig. 1(b). Following this interaction, three consecutive stages are observed:

Phase I. Pre-collision magnetophoresis ($t_{\mathrm{initial}} \leqslant t < t_{\mathrm{contact}}$). During this phase, Droplet 2 moves toward Droplet 1 driven by magnetophoresis. This stage concludes at $t = t_{\mathrm{contact}}$, which we define as the moment of physical contact. By physical contact, we refer to the point at which the undeformed spherical profiles of the two approaching droplets begin to overlap, with a thin liquid film remaining between them. This moment marks the onset of film drainage and the transition to the next phase.

Phase II. Film drainage ($t_{\mathrm{contact}} \leqslant t < t_{\mathrm{coalescence}}$). Upon contact, the droplet pair collectively damps its motion and reaches a quasi-static state, with the contact region centered on the axis of

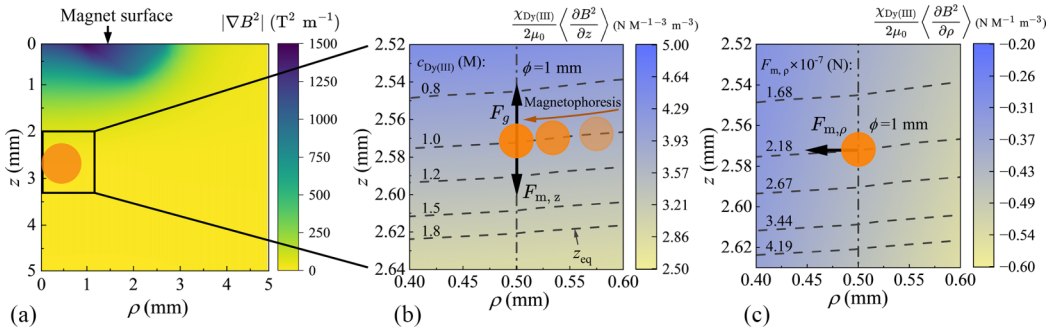


FIG. 2. Numerical modeling of magnetic field and force determination. (a) Spatial distribution of the magnitude of the magnetic pressure gradient $|\nabla B^2|$ in the region of interest, with a superimposed droplet is drawn to scale. (b) Contour map of the vertical magnetic force density [Eq. (2)]. Dashed lines denote the concentration-dependent equilibrium positions z_{eq}, where the upward buoyancy F_g balances the downward Kelvin force $F_{m,z}$ (illustrated by vertical arrows). (c) Corresponding radial force density, where the net compressive force $F_{m,\rho}$ [Eq. (3)] is evaluated along the z_{eq} paths identified in (b). Note: Droplets in (b) and (c) are schematic and not to scale.

symmetry. During this stage, the thin aqueous film confined between the droplet interfaces drains. Coalescence residence time, defined as $\tau_c = t_{coalescence} - t_{contact}$, represents the characteristic time scale of this stage and is the primary focus of this work.

Phase III. Rupture and post-coalescence ($t \geqslant t_{coalescence}$). At $t = t_{coalescence}$, the interfacial film reaches a critical thickness, and rupture occurs. This event leads to rapid coalescence and the subsequent shape relaxation of the merged droplet [43]. While this process is fundamental to the coalescence dynamics, a detailed analysis of the rupture event itself is beyond the scope of the present investigation.

B. The Kelvin force and its scalings

The spatial distribution of the magnetic field generated by the ring-rod magnet configuration [39] was resolved using finite-element analysis (COMSOL MULTIPHYSICS). The minimum mesh element sizes were 10^{-3} mm and 10^{-2} mm in the vertical z and radial ρ directions, respectively. The resulting magnetic field topology is visualized in Fig. 2(a), showing the magnitude of the magnetic pressure gradient ∇B^2, which linearly determines the Kelvin force [Eq. (1)]:

$$\boldsymbol{f}_m = \frac{\chi_{net}}{\mu_0}(\boldsymbol{B}\cdot\nabla)\boldsymbol{B} = \frac{\chi_{net}}{2\mu_0}\nabla B^2, \tag{1}$$

where μ_0 is the vacuum permeability. $\chi_{net} = \chi_{oil} - \chi_{aq}$ represents the volumetric magnetic susceptibility contrast. Since the organic droplets are diamagnetic ($\chi_{oil} \sim 10^{-7}$) and the aqueous phase is strongly paramagnetic due to the Dy(III) ions ($\chi_{aq} \sim 10^{-4}$), the contrast is dominated by the paramagnetic contribution, i.e., $\chi_{net} \approx -\chi_{Dy(III)}c_{Dy(III)}$.

The droplet equilibrium height, z_{eq}, is defined as the distance between the magnet surface and the droplet's center of mass [Fig. 1(b)]. This position is governed by the magneto-Archimedes balance, where the vertical magnetic force counteracts the net buoyancy ($F_{m,z} = \Delta\varrho g V$), as schematically illustrated in Fig. 1(c). To quantify this balance, Fig. 2(b) plots the concentration-normalized vertical force density calculated via Eq. (2):

$$-\frac{F_{m,z}|_{z=z_{eq}}}{c_{Dy(III)}\cdot V} = \frac{\chi_{Dy(III)}}{2\mu_0}\left\langle\frac{\partial B^2}{\partial z}\right\rangle\Big|_{z=z_{eq}}, \tag{2}$$

where the angular brackets $\langle \cdots \rangle$ denote the volume average over the droplet. In Fig. 2(b), the intersection of this force density profile with the buoyancy term (represented by the dashed lines) numerically determines z_{eq} according to Eq. (2). The net radial compressive force $F_{\mathrm{m},\rho}$ that drives the coalescence can be subsequently evaluated via

$$F_{\mathrm{m},\rho} = \int_V \boldsymbol{f}_{\mathrm{m}} \cdot \boldsymbol{e}_\rho \, dV \approx -\frac{\chi_{\mathrm{Dy(III)}}}{2\mu_0} c_{\mathrm{Dy(III)}} V \left\langle \frac{\partial B^2}{\partial \rho} \right\rangle \Bigg|_{z=z_{\mathrm{eq}}}. \tag{3}$$

Figure 2(c) depicts the profile of this volume-averaged radial force density. With Eq. (3), the compressive force during the quasi-static drainage phase is evaluated. Across all Dy(III) concentrations, this yields the scaling $F_{\mathrm{m},\rho} \propto \phi^{4.03}$, as shown in Fig. 1(d). Results for additional variations in viscosity and oil type are provided in Sec. SII B in the Supplemental Material (SM) [44].

It is important to highlight that, due to the orders-of-magnitude difference in magnetic susceptibilities between two phases ($\chi_{\mathrm{aq}} \sim 10^{-4}$ and $\chi_{\mathrm{oil}} \sim 10^{-7}$), any demagnetization effects arising from the geometry changes of the diamagnetic droplets are mathematically negligible. This significant disparity in susceptibilities ensures that the influence of the demagnetization field is minimal and does not impact the system's behavior. Consequently, using the compressive force at the equilibrium position as the driving force for coalescence is fully justified.

III. CORRELATING COALESCENCE RESIDENCE TIME WITH DRAINAGE TIME

A. Characterization of pre-collision magnetophoresis

Prior to collision, Droplet 2 moves under the influence of Kelvin force, buoyancy and hydrodynamic interaction (e.g., viscous drag, virtual mass, or memory force) [42]. The center of Droplet 2 at each frame is extracted using Python/OpenCV scripts (see Sec. SI B in the SM [44]) to determine its trajectory. A differentiation of the droplet trajectory with respect to time yields the local velocity U of the droplet from which the capillary number $\mathrm{Ca} = \mu_{\mathrm{aq}} U/\gamma$ is derived. Both droplets come into physical contact at time t_{contact}, when their center-to-center distance equals their equivalent diameter, $d = \phi_{\mathrm{eq}} = 2\phi_1\phi_2/(\phi_1 + \phi_2)$. t_{contact} is used to scale the timeline so that the collision event now occurs at $t - t_{\mathrm{contact}} = 0$. Figures 3(a) and 3(b), respectively, summarize the statistics of collision angle, θ, and capillary number (Ca) prior to the collision of both droplets for varying droplet diameters. For all droplet sizes, the collision angle θ quickly attains 0° ($\cos\theta = 1$) when the droplets approach each other at $t = t_{\mathrm{contact}}$. This consistently indicates a centrally aligned head-on collision for all experiments conducted. Prior to contact, the droplet's tangential velocity component is negligible which otherwise induces shear flow within the intervening film and alter the drainage dynamics [1,45]. The course of the Capillary number prior to collision is shown in Fig. 3(b). Here, the data for each droplet size is averaged over up to 20 independent repeats. All data collapse onto the same curve with narrow uncertainty bands, indicated as shaded region ($\pm 1\sigma$). These results show that the dynamic evolution toward collision is highly reproducible for all cases.

Furthermore, the kinematics of the approach phase is reflected in the evolution of the dimensionless separation distance h^* (defined alongside the dimensionless time τ^* in Eq. (4), Sec. III B), as depicted in Fig. 3(c). Under the constant Kelvin force, h^* undergoes a rapid decay spanning several orders of magnitude during the approach phase without deformation ($\tau^* < 0$). To directly clarify the coupling between separation and velocity, Fig. 3(d) plots the numerical h^* against the instantaneous Ca, which represents the dimensionless droplet approach velocity. The closer the droplets get to each other, the greater the increase in hydrodynamic drag, causing Ca to drop sharply toward zero. The continuous deceleration ensures that the approach velocity becomes negligible at the onset of contact. This indicates that dynamic pressure variations remain sufficiently small and justifies the subsequent quasi-static drainage analysis for Phase II.

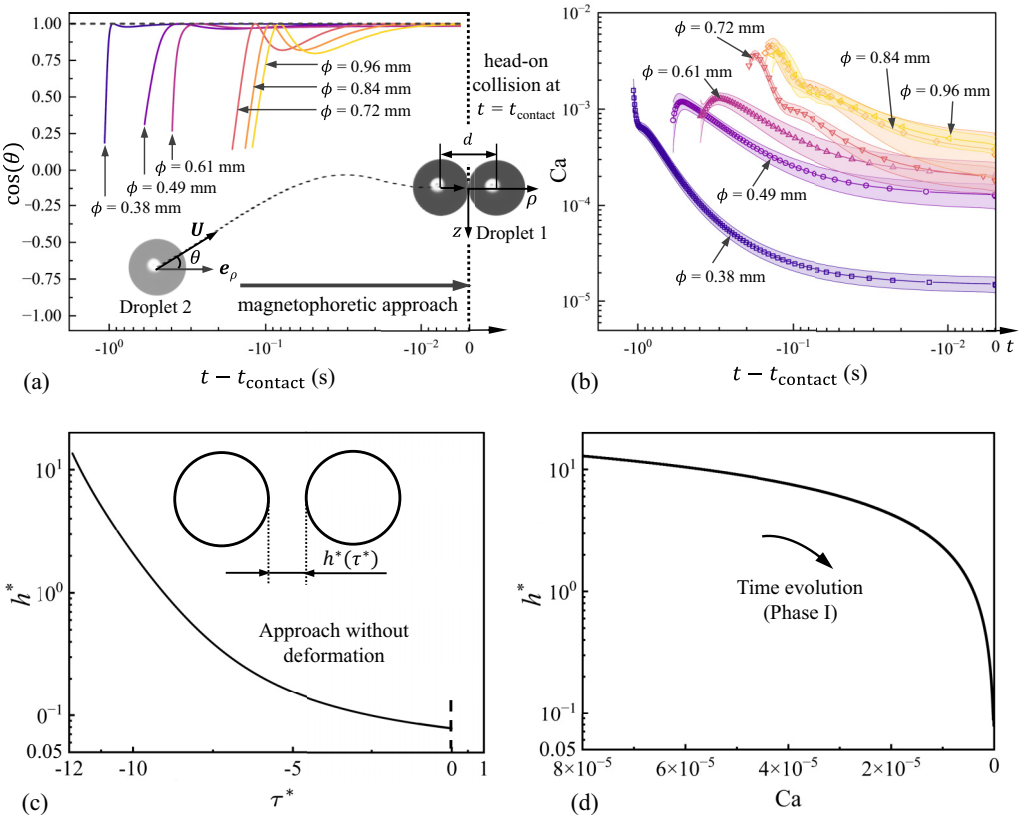


FIG. 3. Characterization of the pre-collision magnetophoresis Phase I of paraffin oil droplets in 1M Dy(III) solution. (a) Cosine of the collision angle θ converging to one, confirming head-on collisions for various droplet diameters ϕ. (b) Temporal evolution of the experimentally measured Capillary number (Ca); shaded regions denote standard deviation ($\pm 1\sigma$). (c) Evolution of the dimensionless separation h^* during the approach phase without deformation ($\tau^* < 0$), with definitions of h^* and τ^* given in Eq. (4). (d) Separation distance h^* versus instantaneous Ca during the pre-collision phase. Note that as the droplets get closer, the increasing hydrodynamic resistance causes a sharp reduction in Ca toward the quasi-static drainage regime ($\tau^* \geqslant 0$).

B. Dimensionless similarity scheme of drainage dynamic

The Stokes-Reynolds-Young-Laplace equation (SRYL-equation) [11,46] describes the drainage dynamics (Phase II) of a liquid film confined in between the two droplets and subjected to externally applied constant normal force. Consistent to experimental observations, we assume a tangentially immobile interfaces. To reveal the independence of the governing physics from specific material properties and length scales, we introduce the following new dimensionless scaling scheme:

$$h^* = h \cdot \frac{\gamma}{F}, \quad \tau^* = \tau \cdot \frac{F}{\phi^2 \cdot \mu_{\text{aq}}}, \quad r^* = r \cdot \frac{\gamma^{1/2}}{\phi^{1/2} \cdot F^{1/2}}, \quad p^* = p \cdot \frac{\phi}{\gamma}, \tag{4}$$

where h, τ, r, and p refer to film height, drainage time, radial axis, and film pressure. The drainage process of thin liquid film between the droplets with immobile interface [12,47]:

$$\frac{\partial h^*(r^*, \tau^*)}{\partial \tau^*} = \frac{1}{12} \cdot \frac{1}{r^*} \frac{\partial}{\partial r^*} \left(r^* h^{*3} \frac{\partial p^*(r^*, \tau^*)}{\partial r^*} \right). \tag{5}$$

The interface deforms in response to the dimensionless film pressure p^*, according to the Young-Laplace equation [25,48,49]

$$p^*(r^*, \tau^*) = 4 - \frac{1}{r^*}\frac{\partial}{\partial r^*}\left(r^*\frac{\partial h^*(r^*, \tau^*)}{\partial r^*}\right). \tag{6}$$

Equation (6) correlates the film pressure p^* to the constant Laplace pressure of the undeformed droplets and the local capillary pressure variation due to the interface deformation. The film pressure, integrated over the entire deformed region, yields the hydrodynamic force that counterbalances the externally applied compressive Kelvin force. This film pressure arises from viscous resistance to film drainage and is expressed in dimensionless form

$$1 = 2\pi \int_0^\infty p^*(r^*, \tau^*) \cdot r^* \, dr^*. \tag{7}$$

The governing equations (5)–(7) are solved with fourth-order finite difference scheme with staggered grid and temporal derivatives approximated by a backward differentiation formula [50].

IV. SCALING LAWS: FROM COALESCENCE RESIDENCE TIME τ_c TO CRITICAL FILM THICKNESS h_{coa}

A. Parameter dependence of the coalescence residence time τ_c

Next, we examine the τ_c dependence on interface aging time, interfacial tension γ, surfactant concentration c_{DeTAB}, viscosity of both phases μ_{aq} and μ_{oil}, diameter ϕ and normal force F. The results are summarized in Fig. 4. Interface aging, Fig. 4(a), refers to the change in interfacial tension during the time when a newly formed interface is exposed to the adsorption of surfactants. To quantify this effect, we define a time, τ_{pre}, that measures the time span in which Droplet 2 is dispersed in the aqueous solution prior to release. The corresponding Droplet 1 has already been dispersed in solution for a much longer period of time. Figure 4(a) shows the correlation between τ_c and τ_{pre} for 0.001 mM DeTAB ($\gamma = 18.93 \pm 1.8$ mN m^{-1}) and 1.0 mM DeTAB ($\gamma = 6.82 \pm 0.3$ mN m^{-1}), respectively, at two droplet diameters ($\phi_{\mathrm{eq}} = 0.49$ and 0.96 mm). Although τ_{pre} spans three orders of magnitudes ($\tau_{\mathrm{pre}} \in [10^0, 10^3]$ s), no obvious surface aging effect on the coalescence residence time τ_c is visible. This observation allows the equilibrium interfacial tension corresponding to the specific DeTAB concentration to be utilized in the subsequent scaling analysis.

Zawala *et al.* [51] noted that for free rising bubbles, a motion-induced dynamic adsorption layer (DAL) can develop during the approach stage and redistribute surfactants, which subsequently modifies the film profile and thickness at contact. While such convective redistribution is characteristic of systems with high Reynolds number (Re = 350−700 in their study) involving bubble bouncing, its influence appears minor in our configuration. Here, the droplets undergo a single head-on collision at a low approach velocity [Ca $\approx 10^{-5} - 10^{-3}$ for various droplet sizes, as shown in Fig. 3(b)], without exhibiting any bouncing behavior. This low-Ca approaching stage, combined with the observed independence of τ_c on τ_{pre} [Fig. 4(a)], suggests that the surfactant distribution governing thin-film drainage is established shortly after droplet formation and remains unaffected by the approach history.

Figure 4(b) summarizes the values of τ_c at varying DeTAB concentration $c_{\mathrm{DeTAB}} \in [10^{-3}, 10^0]$ mM and droplet diameters $\phi \in [0.3, 1]$ mm. The CMC (critical micelle concentration) of DeTAB in 1.0 M Dy(III) is fitted to be around 7.0 mM with the Volmer adsorption isotherm [52], details see Fig. S1 in the SM [44]. The key observation from these data is that the product $\tau_c\gamma$ remains approximately constant across the entire range of c_{DeTAB} and droplet sizes examined. This observed invariance of $\tau_c\gamma$ with respect to variations of the DeTAB concentrations in Fig. 4(b) motivates its use as interfacial tension-normalized coalescence timescale. Additional data for viscosity- and force-controlled variations documented in Sec. SII A in the SM [44] confirm this finding.

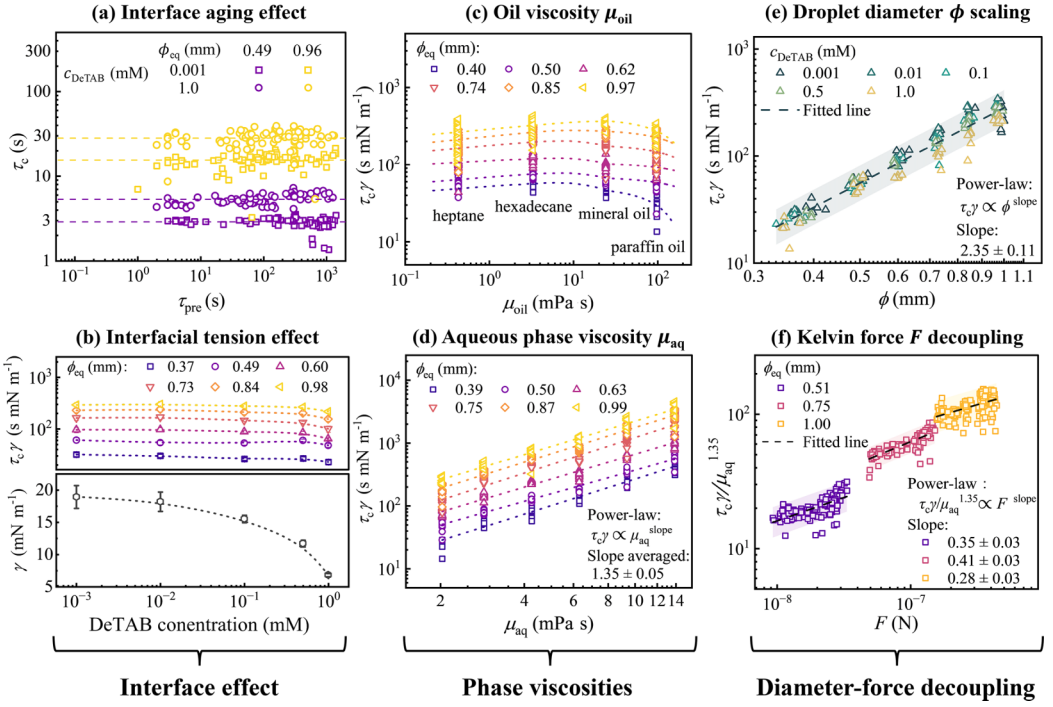


FIG. 4. Parametric scaling analysis of the coalescence residence time τ_c. Columns isolate the effects of interfacial properties (left), phase viscosities (middle), and droplet diameter/force (right). (a), (b) Interfacial effects: (a) independence of τ_c from interface aging time τ_{pre}, and (b) the $\tau_c \propto \gamma^{-1}$ scaling. (c), (d) Viscous effects: $\tau_c\gamma$ is independent of dispersed phase viscosity μ_{oil} in (c) but shows an apparent power law dependence on μ_{aq} across the investigated solution compositions in (d). (e), (f) Size and force effects: Power-law scaling of τ_c with respect to (e) droplet diameter ($\propto \phi^{2.35}$) and (f) the scaling group $\tau_c\gamma/\mu_{aq}^{1.35}$ plotted against the decoupled compressive force ($\propto F^{0.35}$). The shaded area in (e) and (f) represents the 95% prediction interval (PI). For the averaged scaling exponents in (d) and (f), the combined standard deviation is defined as $(\sigma_{in}^2 + \sigma_{between}^2)^{1/2}$ to account for both individual fitting uncertainties (σ_{in}) and variations across independent experimental groups ($\sigma_{between}$). Values indicated in the legends represent nominal droplet diameters; the typical standard deviation across all experimental cases remains within 0.01–0.02 mm (see Sec. SII F in the SM [44] for a detailed size evaluation).

The product $\tau_c\gamma$ shows no discernible dependence on μ_{oil}, which was varied by two orders of magnitude (0.9 mPa s to 97 mPa s) using different oils, see Fig. 4(c). By contrast, it varies systematically with μ_{aq} across the investigated formulations, giving an apparent fitted exponent of 1.35 ± 0.05 as shown in Fig. 4(d).

Classical capillary drainage predicts $\tau_d \propto \mu_{aq}$ when film geometry, forcing, interfacial boundary condition, and rupture criterion are otherwise unchanged [6,11]. Although stochastic rupture can influence film lifetimes in some foaming systems [53], the residence time measured here is drainage-dominated and spans the entire thinning process, from initial contact to film rupture. In Variations 3 and 4, μ_{aq} was changed by varying either the glycerol or Dy(III) concentration. Viscosity and composition were therefore not varied independently. Accordingly, we interpret the fitted value of 1.35 ± 0.05 as an apparent correlation across the investigated formulations, rather than an intrinsic viscosity exponent.

To account for variations in the measured equilibrium interfacial tension (γ), we consider the product ($\tau_c\gamma$). This correction, however, cannot isolate other composition-dependent effects. Previous experiments have reported ion-specific variations in foam-film rupture behavior and lifetime

[54], indicating that electrolyte composition can affect film stability through effects not captured by bulk viscosity alone. More recently, Liu *et al.* showed that electrolyte transport during film thinning can generate concentration gradients and Marangoni stresses that retard coalescence [55]. Gibbs elasticity provides a broader thermodynamic framework for such composition-dependent retardation by linking changes in interfacial composition to changes in surface tension [56]. Talini recently reviewed evidence that equilibrium differences between bulk and surface composition can produce thickness-dependent surface tension and substantially extend film lifetimes in miscible solvent mixtures [57]. Similarly, Henry *et al.* treated surface viscosity as a fitting parameter when comparing film-drainage rates, without attributing the observed differences exclusively to surface viscosity [58]. Although the interfacial geometries differ, these studies identify plausible composition-dependent contributions to film stability in multicomponent systems that may also be relevant to the present oil-aqueous Dy(III) system containing DeTAB. Because our measurements neither determine a Gibbs modulus nor separate these contributions from viscous drainage, we report 1.35 ± 0.05 as an apparent empirical exponent across the investigated formulations.

Figure 4(e) displays the normalized coalescence time, $\tau_c\gamma$, as a function of ϕ. The data exhibit a power-law dependence on ϕ with an apparent exponent of 2.35 ± 0.11. Note that because the applied compressive force F scales with the droplet diameter ϕ as $F \propto \phi^{4.03}$ [see Fig. 1(d)], this exponent of 2.35 is merely a coupled result of both size and force effects. Mathematically, the individual exponents in the scaling relation $\tau_c\gamma \propto \phi^{n_\phi} F^{n_F}$ are subject to the constraint: $n_\phi + 4.03 n_F = 2.35$.

To isolate the individual contributions of ϕ and F, we performed orthogonal experiments in which F was varied by changing Dy(III) concentrations from 0.8 M to 1.8 M for three different droplet size groups ($\phi = 0.5$, 0.75, and 1.0 mm). After accounting for the passively varied viscosity μ_{aq} using the previously derived scaling, Figure 4(f) plots the coalescence residence time, normalized by interfacial tension and viscosity, $\tau_c\gamma/\mu_{aq}^{1.35}$, against F. The correlation reveals a dependence on F with an exponent $n_F = 0.35 \pm 0.05$. Using the apparent diameter constraint and $n_F = 0.35 \pm 0.05$ gives $n_\phi = 0.94 \pm 0.22$. The reported uncertainty of n_ϕ is obtained by propagating the fitted exponent uncertainties in $n_\phi + 4.03 n_F = 2.35$.

B. τ_c scaling law and stochasticity

The summary of the scaling laws found in Sec. IV A yields the following comprehensive scaling law for the coalescence residence time:

$$\frac{\tau_c}{\tau_{c,0}} = \left(\frac{\gamma}{\gamma_0}\right)^{-1} \left(\frac{\mu_{aq}}{\mu_{aq,0}}\right)^{1.35\pm0.05} \left(\frac{\phi}{\phi_0}\right)^{0.94\pm0.22} \left(\frac{F}{F_0}\right)^{0.35\pm0.05}. \tag{8}$$

Here, $\gamma_0 = 18.93$ mN m^{-1}, $\mu_{aq,0} = 2.01$ mPa s, $\phi_0 = 1.00$ mm, and $F_0 = 218.91$ nN are fixed reference values, while $\tau_{c,0} = 13.9$ s is the reference coalescence residence time obtained from the fit. Equation (8) is therefore an empirical reference-normalized correlation for the parameter ranges investigated here. It summarizes the observed change in τ_c after accounting for measured changes in the equilibrium interfacial tension γ. However, the remaining apparent viscosity dependence cannot be attributed to a specific interfacial mechanism on the basis of this correlation alone, and the resulting dimensionless ratios are not intended as similarity groups derived from a mechanistic theory.

Empirical power laws with noninteger and system dependent exponents are commonly used to describe liquid-liquid coalescence data [6]. Equation (8) combines the exponents obtained from the sequential fits described above. The resulting correlation is compared with all 1650 coalescence events from the four parameter variations. The coalescence times fitted by Eq. (8), $\tau_{c,fit}$, are plotted against the experimentally measured time, $\tau_{c,exp}$, for 1650 data points across all discussed variations. As shown in Fig. 5(a), for varying concentrations and varying viscosities see Fig. 5(b), the data points collapse onto the line of identity ($y = x$). This indicates a good agreement across the entire experimental domain. Hence, this scaling is valid within a continuous phase viscosity

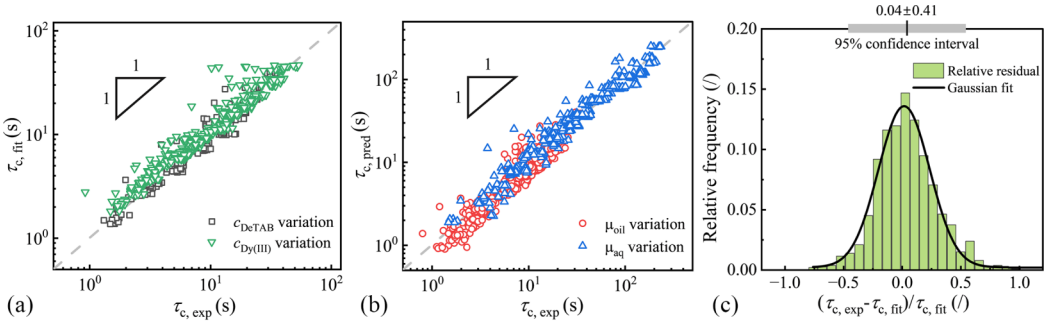


FIG. 5. (a), (b) Coalescence residence time calculated using Eq. (8), $\tau_{c,fit}$, versus measured value $\tau_{c,exp}$ for the concentration and viscosity variations, respectively. (c) Histogram of the relative frequency of $(\tau_{c,exp} - \tau_{c,fit})/\tau_{c,fit}$ exhibiting a Gaussian distribution.

range of $\mu_{aq} \in [1.8, 14]$ mPa s, while τ_c remains unaffected by variations in the dispersed phase viscosity $\mu_{oil} \in [0.9, 98]$ mPa s. The validated parameter space further spans droplet diameters $\phi \in [0.3, 1.0]$ mm and compressive forces $F \in [2.6, 440]$ nN, demonstrating its applicability within the investigated regime. Equation (8) further incorporates the measured interfacial tension and the apparent aqueous phase viscosity correlation, providing an empirical parametrization within the investigated formulations. Figure 5(c) summarizes the statistics for the relative residuals of measured τ_c compared to the scaling model, defined as $(\tau_{c,exp} - \tau_{c,fit})/\tau_{c,fit}$. The relative residual distribution is well approximated by a Gaussian distribution rather than a stochastic distribution.

To compare our findings with those reported in the literature, Table II summarizes the existing scaling laws. All scaling laws for τ_c predict a power-law dependency on droplet size and external compressive force, represented by the Kelvin force in our study. However, they exhibit noticeable differences in the exponents of their respective variables.

In Table II, viscosity is incorporated through source-specific nondimensional times based on a viscous capillary scale. The remaining groups reflect the force $\bar{F}$, Hamaker constant A, viscosity ratio λ, and rupture scalings h adopted in each model. For example, the relation of Frostad *et al.* includes a critical rupture thickness that itself depends on force and the dimensionless Hamaker constant [5]. None of the cited studies independently determined a continuous-phase viscosity

TABLE II. Comparison of coalescence time scaling laws. Here, τ_c^* and τ_c denote the dimensionless and dimensional coalescence residence times, respectively. For consistency, all scaling laws are formulated in terms of droplet diameter ϕ and force F. The dimensionless groups follow source-specific definitions rescaled to ϕ, i.e., $\tau_c^* = \tau_c\gamma/(\mu\phi)$, $\bar{F} = F/(\gamma\phi)$, $A = A_H/(\gamma\phi^2)$, and λ denotes the viscosity ratio. The 'reported dependence' column lists only proportional relationships, with prefactors omitted, to facilitate comparison of the scaling exponents. The correlation developed in the present study is given in the dimensionally consistent, reference-normalized form of Eq. (8).

Source	Nondimensional τ_c^*	Dependence of τ_c	Interface	Configuration	Approach
Charles & Mason [13]	$\bar{F}^{2/3}A^{-2/3}$	$F^{2/3}\phi^{5/3}$	Immobile	Drop-flat	Lubrication theory
Chesters [1]	$\lambda\bar{F}^{1/3}A^{-1/3}$	$F^{1/3}\phi^{4/3}$	Mobile	Drop-drop	Asymptotic analysis
Nemer *et al.* [59]	$\lambda\bar{F}^{13/24}A^{-5/12}$	$F^{13/24}\phi^{31/24}$	Mobile	Drop-drop	Asymptotic analysis
Chen *et al.* [60]	$\bar{F}^{1/2}A^{-1/2}$	$F^{1/2}\phi^{3/2}$	Immobile	Drop-flat	Stability analysis
Frostad *et al.* [61]	$\bar{F}^{1/4}A^{-1/2}$	$F^{1/4}\phi^{7/4}$	Immobile	Drop-drop	Scaling analysis
Frostad *et al.* [5]		$F^{0.05}\phi^{1.78}$	Immobile	Drop-drop	CCFA experiment
This work: Eq. (8)		$F^{0.35}\phi^{0.94}\,\gamma^{-1}\mu_{aq}^{1.35}$	Immobile	Drop-drop	Contactless experiment

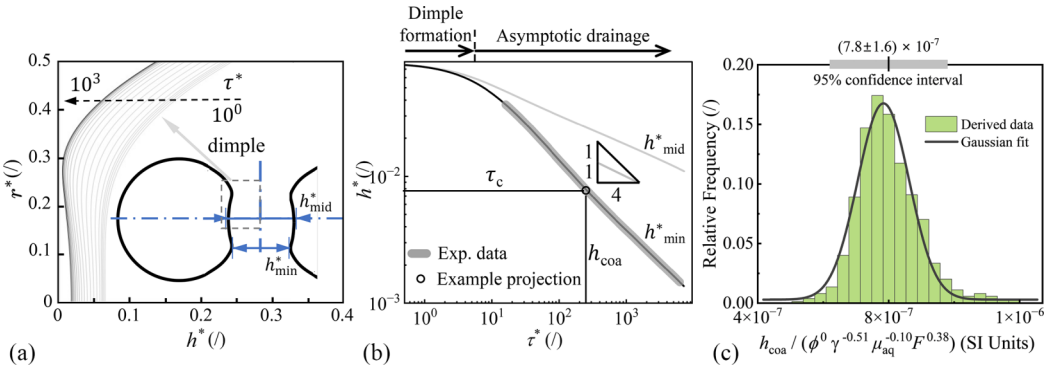


FIG. 6. Drainage dynamics in nondimensional units: (a) Spatiotemporal evolution of the film thickness along the radial coordinates r^*, shown for discrete time steps τ^*. The inset schematically illustrates the dimpled interface geometry, defining the central (h^*_{mid}) and minimum (h^*_{min}) film thicknesses. (b) Temporal evolution of both quantities, which decay as power laws over time τ^* with exponents of $-1/4$ and $-1/2$, respectively. The experimentally measured τ_c, in dimensionless units, is mapped onto the h^*_{min} evolution curve, where it is shown as the thick solid line segment, to derive the corresponding critical film thickness (h_{coa}). (c) The critical film thickness obeys the scaling $h_{\mathrm{coa}} \propto \phi^0 \gamma^{-0.51} \mu_{\mathrm{aq}}^{-0.10} F^{0.38}$ and exhibits a Gaussian distribution.

exponent by fitting experimental data. Table II is, therefore, used solely to compare the reported force and droplet-size dependences.

It should be noted that all scaling laws published to date predict a stronger dependence on droplet diameter than was observed in this study ($\tau_c \propto \phi^{0.94}$). In addition, our observed force exponent ($\tau_c \propto F^{0.35}$) is weaker than the classical prediction for immobile, flat films, $F^{2/3}$ by Charles and Mason [13] and $F^{1/2}$ by Chen *et al.* [60], but similar to the prediction of Chesters [1] for mobile interfaces ($F^{1/3}$). In contrast, Frostad *et al.* [5] reported a much weaker force dependence ($\tau_c \sim F^{0.05}$) using a cantilevered capillary force apparatus (CCFA), suggesting that classical models might overestimate the role of the force. However, we propose that this discrepancy may stem from the fundamental difference in the application of the force. In their previous theoretical framework, Frostad *et al.* [61] derived $\tau_c \sim F^{1/4}$ for drops interacting under a constant force. On the one hand, the CCFA apparatus enables precise force control. On the other hand, the capillary exerts a localized force that can lead to an overall deformation of the droplets. This is an obvious difference to this work, where the Kelvin force is distributed over a larger interfacial area. Note the compressive Kelvin force in our case matches closely the boundary conditions in classical theories [61,62]. Hence, the force dependence in our study ($F^{0.35}$) is closer to that predicted with theoretical consensus ($F^{1/3}$–$F^{1/2}$) rather than the invasive measurement results. We also note again that the statistics of τ_c determined experimentally by Frostad *et al.* [5] exhibit a size-dependent stochasticity. The coalescence residence times transit from deterministic distribution (a variability of $\sim 5\% - 10\%$) for droplets with a diameter of <0.2 mm to a relatively flat distribution for droplets with a diameter of 0.3 mm. This transition was attributed to the increased sensitivity of coalescence time to film thickness perturbations ($|d\tau_c/dh| \sim \phi^{1.58}$). In our study, the relative residual statistics in Fig. 5(c) reveals a Gaussian distribution. Using the τ_c scaling law, the following subsection examines the stochasticity of critical film thickness that mark the end of coalescence residence time.

C. h_{coa} scaling law and stochasticity

Figure 6(a) quantifies the deformation of the droplet interface in Phase II using the dimensionless scheme established in Sec. III B. The evolution of the liquid film profile h^* along dimensionless radial axis r^* is depicted at exponentially increasing time steps τ^*. At the end of pre-collision phase at $\tau^* = 0$, the interface start to deform where a dimpled interface forms rather quickly, cf. Fig. 6(a).

TABLE III. Comparison of derived scaling exponents for the critical coalescence thickness h_{coa} based on the previous existing theoretical predictions and current work. The values indicate the power-law dependency of h_{coa} on each physical variable.

Source	F	ϕ	γ	μ_{aq}	Film condition
Vrij [19]	0.25	0.25	−0.50		Nonthinning, plane-parallel, homogeneous; Thermal fluctuation growth only
Radoev *et al.* [22]	0	0.08	−0.40	0.11	Thinning, plane-parallel, nonhomogeneous; Static wave growth rate
Sharma & Ruckenstein [64,65]	0	0.10	−0.36	0.13	Thinning film, temporal oscillating; Coupled wave growth and drainage
Frostad *et al.* [5] Eqs. (4)–(5)	0.17	0.17	−0.50	0	Thinning, dimpled; Radially bounded geometry
This work: Eq. (9)	0.38	0	−0.50	−0.10	Thinning, dimpled; Predicted by measured τ_c and lubrication theory

The interface dimpling evolves rapidly at the early stages, whereas the subsequent drainage proceeds at a much reduced speed. We extract the interface distance between droplets at the film center, h^*_{mid}, and the smallest distance between the droplets, h^*_{min}, as a function of time in Fig. 6(b). Note the power law correlation $h^*_{min} \propto (\tau^*)^{-1/2}$ and $h^*_{mid} \propto (\tau^*)^{-1/4}$ are correctly captured during the asymptotic drainage stage, consistent with the conclusions derived from asymptotic analysis by Davis and coworkers [62,63].

Governed by the dimensionless scheme introduced, the drainage dynamics is independent on the physical properties, length and time. Therefore, the experimentally measured coalescence time τ_c can be projected on h^*_{min} which is the minimum film thickness at progressive time τ^* in Fig. 6(b). First, we identify the dimensionless time at which coalescence occurs, assuming drainage begins at $\tau^* = 0$. Important to note that coalescence takes place in the asymptotic regime for all cases considered. Hence, the τ^* interval prior to dimple formation represents only a small fraction of the entire drainage duration. This validates the approximation that the beginning of measured drainage process (left margin of τ^*_c) overlaps that of the numerical one ($\tau^* = 0$) when the dimple formation starts. Then, we extract h^*_{coa} by propagating the experimental points on the drainage master curve to the vertical axis and re-dimensionalizing with the time scaling factor in Eq. (4) (details in Sec. SII C in the SM [44]). For that purpose, we use the dimensionless scheme cf. Eq. (4),

$$\tau^*_c = \tau_c \cdot \frac{F}{\phi^2 \cdot \mu_{aq}} \quad \Rightarrow \quad \tau^*_c \mapsto h^*_{min} = f(\tau^*_c) \quad \Rightarrow \quad h_{coa} = h^*_{min} \cdot \frac{F}{\gamma},$$

to calculate the thickness of h_{coa} when coalescence takes place. Remarkably, this dimensional rupture thickness h_{coa} exhibits a power-law scaling:

$$\frac{h_{coa}}{h_{coa,0}} = \left(\frac{\gamma}{\gamma_0}\right)^{-0.51} \left(\frac{\mu_{aq}}{\mu_{aq,0}}\right)^{-0.10} \left(\frac{F}{F_0}\right)^{0.38}. \tag{9}$$

$h_{coa} \in [3.4, 63.4]$ nm is the film thickness derived at which the film ruptures and coalescence occurs. $h_{coa,0} = 32.3$ nm is the reference rupture thickness obtained from the fit at the same γ_0, $\mu_{aq,0}$, and F_0 defined below Eq. (8). Equation (9) is, therefore, an empirical reference-normalized correlation for the parameter ranges investigated here. This value is (1...2) orders of magnitude larger than the Debye length ($\kappa^{-1} \approx 0.09$–0.14 nm, see Eq. (S5) in the SM [44]) for Dy(III) solutions in the range from 0.8 M to 1.8 M. Therefore, the magnitude of h_{coa} emphasizes that repulsive double layer forces are negligible throughout the entire drainage process till coalescence. Table III compares

previously reported theoretical scaling relations for h_{coa} with that of this work in Eq. (9) with detailed derivations in Sec. SII D in the SM [44].

Equations (10)–(12) reproduce source-specific proportional dependences with their dimensional prefactors omitted and are included only to compare the reported exponents. Based on Scheludko's theory of film instability [18], Vrij [19] proposed a stationary thermal fluctuation growth model for film rupture. Under the same premise of negligible repulsive disjoining pressure due to electric double layer interaction and a constant Hamaker constant, this model predicts the critical film thickness to scale according to

$$h_{coa} \propto F^{0.25}\phi^{0.25}\gamma^{-0.50}, \tag{10}$$

obtained by introducing the dimensionless factors in Eq. (4) into Vrij's model [19] [Eq. (7.6)]. Taking film thinning speed into account, Radoev *et al.* [22] [Eq. (18′)] extended Vrij's static model incorporating film thinning velocity, yielding

$$h_{coa} \propto \gamma^{-0.30}\mu^{-0.20}V_{Re}^{-0.20}. \tag{11}$$

Sharma & Ruckenstein [64,65] [Eq. (42)] further incorporated hydrodynamic damping of thermal waves during thinning, predicting

$$h_{coa} \propto \gamma^{-0.24}\mu^{-0.24}V_{Re}^{-0.24}\xi_0^{0.04}, \tag{12}$$

where ξ_0 is the amplitude of thermal perturbation.

The experimentally measured dependence $h_{coa} \propto \gamma^{-0.51}$ in this work agrees closely with the quasi-static stability models of Vrij [19] and Frostad *et al.* [5]. This suggests that the film rupture in the present system might be initiated by thermal fluctuations, a conclusion further supported by recent molecular dynamics simulation [66]. Chireux *et al.* [67] experimentally demonstrated that the minimum distance between droplets ($\phi \geqslant 4$ μm) in air at which the jump-to-contact and coalescence occurs, scales as $d_{min} \propto \gamma^{-1/2}$. This suggests that, even when accounting for the viscous effect of the carrier media and the contact area deformation as in our system, the film rupture event is ultimately determined by the vdW forces, provided that electric double layer forces are absent. These interpretations are also consistent with a recent scaling analysis by Chatzigiannakis and Vermant [68] which predicts

$$h_{coa} \approx h_{coa,Vrij}(1 + Ca)^{2/7}, \tag{13}$$

where $h_{coa,Vrij}$ is the critical film thickness predicted by Vrij's model. Under the present low-Ca condition ($Ca \leqslant 10^{-3}$), hydrodynamic damping becomes small, causing the rupture mechanism to converge toward the static Vrij regime while retaining signatures of dynamic drainage. At the same time, the exponents for force, droplet diameter and dynamic viscosity obtained in the scaling of the critical film thickness above differ from those predicted theoretically. This indicates that none of the available theories to date simultaneously account for force-controlled drainage, dimpled interfaces together with rupture inferred from that measured experimentally.

V. DISCUSSION AND CONCLUSION

We establish a systematic framework to quantify both the coalescence residence time and the critical film thickness of droplets subject to a constant, contactless normal compressive force. By explicitly linking macroscopic residence time to the underlying drainage dynamics, this framework bridges the gap between hydrodynamic drainage and microscopic interface rupture. The approach is validated for millimeter-scale, equal-sized oil droplets dispersed in a highly concentrated aqueous phase in the presence of water soluble surfactant. The resulting scaling law for the coalescence residence time, Eq. (8), proves robust across a wide parameter space, spanning two orders of magnitude in dispersed phase viscosity ($\mu_{oil} \in [0.9, 97]$ mPa s), continuous phase viscosity ($\mu_{aq} \in [1.8, 14]$ mPa s), and compressive forces ($F \in [2.6, 440]$ nN).

Building on these results, we propose a dimensionless similarity framework that unifies the drainage dynamics onto a single, master curve, independent of fluid properties, droplet size, forces, characteristic lengths, and time scales. This framework allows the experimentally measured residence time to be mapped onto a master curve representing the evolution of the dimensionless minimum film thickness over time during drainage. Consequently, the critical film thickness, h_{coa}, is inferred across a broad range of initial conditions and system parameters from the corresponding experiments.

Based on this approach, a scaling law of h_{coa}, Eq. (9), is derived and substantiated by a robust Gaussian distribution. We find that h_{coa} follows a power law dependence on interfacial tension $\propto \gamma^{-0.51}$. From the microscopic perspective, this relationship suggests that thermal fluctuation-induced film rupture, as described by Vrij's theory, can partially explain the destabilization mechanism. However, further theoretical modeling tailored specifically to force-controlled, dimpled drainage is required to fully capture these experimentally relevant conditions.

Beyond the specific fluids validated here, our framework is broadly applicable to complex multiphase systems with diverse material properties, particularly those involving surface-active species and ionic environments typical of industrial processes. In the context of state-of-the-art rare-earth hydrometallurgy [8,69–71], efficient demulsification through enhanced coalescence is vital for improving material recovery. By providing a solid foundation for optimizing demulsification, this framework creates a strong synergy with magnetically assisted extraction kinetics [72,73], offering a viable technical pathway toward highly efficient, next-generation rare-earth separation and recycling technologies.

ACKNOWLEDGMENTS

We are grateful for the financial support of the German Aerospace Center (DLR) with funds provided by the Federal Ministry for Economic Affairs and Energy (BMWi) due to an enactment of the German Bundestag under Grant No. DLR 50WM2359 (Project Magsolex II). We acknowledge the German Federal Ministry of Research, Technology and Space (BMFTR) with funds provided in the context of DATIPilot-Sprint under Grant No. 03DPS1187 (Project KepRE).

DATA AVAILABILITY

Raw data used in this study are provided in the manuscript and Supplemental Material. Additional data supporting the findings are available from the corresponding author upon reasonable request.

[1] A. K. Chesters, Modelling of coalescence processes in fluid-liquid dispersions: A review of current understanding, Chem. Eng. Res. Des. **69**, 259 (1991).

[2] T. F. Tadros, Emulsion formation, stability, and rheology, in *Emulsion Formation and Stability*, edited by T. F. Tadros (Wiley-VCH, Weinheim, Germany, 2013), pp. 1–75.

[3] B. P. Binks, *Modern Aspects of Emulsion Science* (Royal Society of Chemistry, Cambridge, UK, 2007).

[4] H. R. Pruppacher and J. D. Klett, *Microphysics of Clouds and Precipitation: Reprinted 1980* (Springer, Dordrecht, 2012).

[5] J. M. Frostad, A. Paul, and L. G. Leal, Coalescence of droplets due to a constant force interaction in a quiescent viscous fluid, Phys. Rev. Fluids **1**, 033904 (2016).

[6] J. Kamp, J. Villwock, and M. Kraume, Drop coalescence in technical liquid/liquid applications: A review on experimental techniques and modeling approaches, Rev. Chem. Eng. **33**, 1 (2017).

[7] L. Leal, Flow induced coalescence of drops in a viscous fluid, Phys. Fluids **16**, 1833 (2004).

[8] F. Xie, T. A. Zhang, D. Dreisinger, and F. Doyle, A critical review on solvent extraction of rare earths from aqueous solutions, Miner. Eng. **56**, 10 (2014).
[9] J. Rydberg, *Solvent Extraction Principles and Practice, Revised and Expanded* (CRC Press, Boca Raton, FL, 2004).
[10] H. A. Stone, Dynamics of drop deformation and breakup in viscous fluids, Annu. Rev. Fluid Mech. **26**, 65 (1994).
[11] D. Y. Chan, E. Klaseboer, and R. Manica, Film drainage and coalescence between deformable drops and bubbles, Soft Matter **7**, 2235 (2011).
[12] O. Reynolds, IV. On the theory of lubrication and its application to Mr. Beauchamp Tower's experiments, including an experimental determination of the viscosity of olive oil, Philos. Trans. R. Soc. London 157 (1886).
[13] G. E. Charles and S. G. Mason, The coalescence of liquid drops with flat liquid/liquid interfaces, J. Colloid Sci. **15**, 236 (1960).
[14] S. Hartland, The approach of a liquid drop to a flat plate, Chem. Eng. Sci. **22**, 1675 (1967).
[15] S. Hartland, The profile of the draining film between a rigid sphere and a deformable fluid-liquid interface, Chem. Eng. Sci. **24**, 987 (1969).
[16] S. Hartland, The profile of the draining film between a fluid drop and a deformable fluid-liquid interface, Chem. Eng. J. **1**, 67 (1970).
[17] G. Jeffreys and G. Davies, Coalescence of liquid droplets and liquid dispersion, in *Recent Advances in Liquid–Liquid Extraction*, edited by C. Hanson (Pergamon Press, Oxford, UK, 1971), pp. 495–584.
[18] A. Scheludko, Sur certaines particularités des lames mousseuses. ii. stabilité cinétique, épaisseur critique et épaisseur d'équilibre, Proc. K. Ned. Akad. Wet. Ser. B **65**, 87 (1962).
[19] A. Vrij, Possible mechanism for the spontaneous rupture of thin, free liquid films, Discuss. Faraday Soc. **42**, 23 (1966).
[20] I. Ivanov, B. Radoev, E. Manev, and A. Scheludko, Theory of the critical thickness of rupture of thin liquid films, Trans. Faraday Soc. **66**, 1262 (1970).
[21] I. B. Ivanov and P. A. Kralchevsky, Stability of emulsions under equilibrium and dynamic conditions, Colloids Surf. A **128**, 155 (1997).
[22] B. P. Radoev, A. D. Scheludko, and E. D. Manev, Critical thickness of thin liquid films: Theory and experiment, J. Colloid Interface Sci. **95**, 254 (1983).
[23] V. V. Tarasov and G. A. Yagodin, Interfacial phenomena in solvent extraction, in *Ion Exchange and Solvent Extraction: A Series of Advances*, edited by J. A. Marinsky and Y. Marcus (Marcel Dekker, New York, 1988), Vol. 10, pp. 141–237.
[24] S. G. Yiantsios and R. H. Davis, On the buoyancy-driven motion of a drop towards a rigid surface or a deformable interface, J. Fluid Mech. **217**, 547 (1990).
[25] E. Klaseboer, J. P. Chevaillier, C. Gourdon, and O. Masbernat, Film drainage between colliding drops at constant approach velocity: Experiments and modeling, J. Colloid Interface Sci. **229**, 274 (2000).
[26] B. Dai and L. G. Leal, The mechanism of surfactant effects on drop coalescence, Phys. Fluids **20**, 040802 (2008).
[27] S. Narayan, I. Makhnenko, D. B. Moravec, B. G. Hauser, A. J. Dallas, and C. S. Dutcher, Insights into the microscale coalescence behaviorof surfactant-stabilized droplets using a microfluidic hydrodynamictrap, Langmuir **36**, 9827 (2020).
[28] H. Yang, C. C. Park, Y. T. Hu, and L. G. Leal, The coalescence of two equal-sized drops in a two-dimensional linear flow, Phys. Fluids **13**, 1087 (2001).
[29] W. Bartok and S. Mason, Particle motions in sheared suspensions: VIII. Singlets and doublets of fluid spheres, J. Colloid Sci. **14**, 13 (1959).
[30] J. M. Frostad, M. C. Collins, and L. G. Leal, Cantilevered-capillary force apparatus for measuring multiphase fluid interactions, Langmuir **29**, 4715 (2013).
[31] P. Rehbinder and E. Wenström, Stabilisierende wirkung von adsorptionsschichten grenzflächenaktiver stoffe auf disperse systeme. II. Stabilität von blasen und tropfen an trennungsflächen, Kolloid-Z. **53**, 145 (1930).

[32] B. Deryagin and M. Kussakov, Anomalous properties of thin polymolecular films. V, Acta Physicochim. URSS **10**, 25 (1939).
[33] E. Cockbain and T. McRoberts, The stability of elementary emulsion drops and emulsions, J. Colloid Sci. **8**, 440 (1953).
[34] A. Sheludko, Thin liquid films, Adv. Colloid Interface Sci. **1**, 391 (1967).
[35] D. Tabor and R. S. Winterton, The direct measurement of normal and retarded van der Waals forces, Proc. R. Soc. London A **312**, 435 (1969).
[36] G. Binnig, C. F. Quate, and C. Gerber, Atomic force microscope, Phys. Rev. Lett. **56**, 930 (1986).
[37] N. H. Sagert and M. J. Quinn, The coalescence of n-hexane droplets in aqueous electrolyte solutions, Can. J. Chem. Eng. **56**, 679 (1978).
[38] M. Yokota and K. Okumura, Dimensional crossover in the coalescence dynamics of viscous drops confined in between two plates, Proc. Natl. Acad. Sci. USA **108**, 6395 (2011).
[39] Z. Lei, B. Fritzsche, R. Salikhov, K. Schwarzenberger, O. Hellwig, and K. Eckert, Magnetic separation of rare-earth ions: Property database and Kelvin force distribution, J. Phys. Chem. C **126**, 2226 (2022).
[40] E. Beaugnon and R. Tournier, Levitation of organic materials, Nature (London) **349**, 470 (1991).
[41] Z. Lei, B. Fritzsche, and K. Eckert, Stability criterion for the magnetic separation of rare-earth ions, Phys. Rev. E **101**, 013109 (2020).
[42] Y. He, K. Ortmann, K. Eckert, and Z. Lei, Rectilinear magnetophoresis of a single oil droplet in a paramagnetic rare-earth solution, Phys. Rev. Fluids **10**, 033603 (2025).
[43] J. Eggers, J. R. Lister, and H. A. Stone, Coalescence of liquid drops, J. Fluid Mech. **401**, 293 (1999).
[44] See Supplemental Material at http://link.aps.org/supplemental/10.1103/8tjf-ky6v for detailed descriptions of solution preparation, interfacial tension characterization, the OpenCV droplet tracking method, and mathematical derivations of asymptotic film drainage, which includes Refs. [74–86].
[45] L. G. Leal, *Advanced Transport Phenomena: Fluid Mechanics and Convective Transport Processes* (Cambridge University Press, Cambridge, 2007), Vol. 7.
[46] R. Manica and D. Y. Chan, Drainage of the air–water–quartz film: Experiments and theory, Phys. Chem. Chem. Phys. **13**, 1434 (2011).
[47] A. Jones and S. Wilson, The film drainage problem in droplet coalescence, J. Fluid Mech. **87**, 263 (1978).
[48] D. Chappelear, Models of a liquid drop approaching an interface, J. Colloid Sci. **16**, 186 (1961).
[49] R. Finn, *Equilibrium Capillary Surfaces* (Springer, New York, NY, 2012), Vol. 284.
[50] S. D. Cohen, A. C. Hindmarsh, and P. F. Dubois, CVODE, a stiff/nonstiff ODE solver in C, Comput. Phys. **10**, 138 (1996).
[51] J. Zawala, J. Miguet, P. Rastogi, O. Atasi, M. Borkowski, B. Scheid, and G. G. Fuller, Coalescence of surface bubbles: The crucial role of motion-induced dynamic adsorption layer, Adv. Colloid Interface Sci. **317**, 102916 (2023).
[52] N. I. Politova, S. Tcholakova, S. Tsibranska, N. D. Denkov, and K. Muelheims, Coalescence stability of water-in-oil drops: Effects of drop size and surfactant concentration, Colloids Surf. A **531**, 32 (2017).
[53] W. Drenckhan and A. Saint-Jalmes, The science of foaming, Adv. Colloid Interface Sci. **222**, 228 (2015).
[54] S. I. Karakashev, P. T. Nguyen, R. Tsekov, M. A. Hampton, and A. V. Nguyen, Anomalous ion effects on rupture and lifetime of aqueous foam films formed from monovalent salt solutions up to saturation concentration, Langmuir **24**, 11587 (2008).
[55] B. Liu, R. Manica, Q. Liu, Z. Xu, E. Klaseboer, and Q. Yang, Nanoscale transport during liquid film thinning inhibits bubble coalescing behavior in electrolyte solutions, Phys. Rev. Lett. **131**, 104003 (2023).
[56] M. v. d. Tempel, J. Lucassen, and E. Lucassen-Reynders, Application of surface thermodynamics to Gibbs elasticity, J. Phys. Chem. **69**, 1798 (1965).
[57] L. Talini, Lifetimes of films, bubbles, and foams in mixtures of non-aqueous solvents, Curr. Opin. Colloid Interface Sci. **83**, 102018 (2026).
[58] C. L. Henry, S. I. Karakashev, P. T. Nguyen, A. V. Nguyen, and V. S. Craig, Ion specific electrolyte effects on thin film drainage in nonaqueous solvents propylene carbonate and formamide, Langmuir **25**, 9931 (2009).

[59] M. B. Nemer, X. Chen, D. H. Papadopoulos, J. Bławzdziewicz, and M. Loewenberg, Comment on "two touching spherical drops in uniaxial extensional flow: Analytic solution to the creeping flow problem", J. Colloid Interface Sci. **308**, 1 (2007).
[60] J.-D. Chen, P. S. Hahn, and J. Slattery, Coalescence time for a small drop or bubble at a fluid-fluid interface, AIChE J. **30**, 622 (1984).
[61] J. Frostad, J. Walter, and L. Leal, A scaling relation for the capillary-pressure driven drainage of thin films, Phys. Fluids **25**, 052108 (2013).
[62] S. G. Yiantsios and R. H. Davis, Close approach and deformation of two viscous drops due to gravity and van der Waals forces, J. Colloid Interface Sci. **144**, 412 (1991).
[63] R. H. Davis, J. A. Schonberg, and J. M. Rallison, The lubrication force between two viscous drops, Phys. Fluids **1**, 77 (1989).
[64] A. Sharma and E. Ruckenstein, Critical thickness and lifetimes of foams and emulsions: Role of surface wave-induced thinning, J. Colloid Interface Sci. **119**, 14 (1987).
[65] A. Sharma and E. Ruckenstein, Stability, critical thickness, and the time of rupture of thinning foam and emulsion films, Langmuir **3**, 760 (1987).
[66] S. Perumanath, M. K. Borg, M. V. Chubynsky, J. E. Sprittles, and J. M. Reese, Droplet coalescence is initiated by thermal motion, Phys. Rev. Lett. **122**, 104501 (2019).
[67] V. Chireux, M. Protat, F. Risso, T. Ondarçuhu, and P. Tordjeman, Jump-to-contact instability: The nanoscale mechanism of droplet coalescence in air, Phys. Rev. Fluids **3**, 102001(R) (2018).
[68] E. Chatzigiannakis and J. Vermant, Breakup of thin liquid films: From stochastic to deterministic, Phys. Rev. Lett. **125**, 158001 (2020).
[69] K. M. Goodenough, F. Wall, and D. Merriman, The rare earth elements: Demand, global resources, and challenges for resourcing future generations, Nat. Resour. Res. **27**, 201 (2018).
[70] T. Cheisson and E. J. Schelter, Rare earth elements: Mendeleev's bane, modern marvels, Science **363**, 489 (2019).
[71] V. Balaram, Rare earth elements: A review of applications, occurrence, exploration, analysis, recycling, and environmental impact, Geosci. Front. **10**, 1285 (2019).
[72] K. Ortmann, A. Bidmon, K. Eckert, and Z. Lei, Increasing rare earth extraction kinetics by tailored magnetic fields, Commun. Phys. **8**, 427 (2025).
[73] Y. He, A. Bidmon, X. Lu, K. Eckert, and Z. Lei, Quantifying dysprosium extraction kinetics via magnetic levitation, Chem. Eng. J. **535**, 175382 (2026).
[74] S. Arrhenius, Über die innere reibung verdünnter wässeriger lösungen, Z. Phys. Chem. **1U**, 285 (1887).
[75] G. Bradski and A. Kaehler, The OpenCV Library, Dr. Dobb's J. Software Tools **25**, 120 (2000).
[76] N.-S. Cheng, Formula for the viscosity of a glycerol-water mixture, Ind. Eng. Chem. Res. **47**, 3285 (2008).
[77] T. Cosgrove, *Colloid Science: Principles, Methods and Applications* (John Wiley & Sons, New York, 2010).
[78] V. S. Craig, Bubble coalescence and specific-ion effects, Curr. Opin. Colloid Interface Sci. **9**, 178 (2004).
[79] D. B. Hough and L. R. White, The calculation of Hamaker constants from Liftshitz theory with applications to wetting phenomena, Adv. Colloid Interface Sci. **14**, 3 (1980).
[80] J. N. Israelachvili, *Intermolecular and Surface Forces* (Academic Press, New York, 2011).
[81] G. Jones and M. Dole, The viscosity of aqueous solutions of strong electrolytes with special reference to barium chloride, J. Am. Chem. Soc. **51**, 2950 (1929).
[82] M. Kaminsky, Ion-solvent interaction and the viscosity of strong-electrolyte solutions, Discuss. Faraday Soc. **24**, 171 (1957).
[83] G. M. Kontogeorgis and S. Kiil, *Introduction to Applied Colloid and Surface Chemistry* (John Wiley & Sons, New York, 2016).
[84] W. Kunz, P. L. Nostro, and B. W. Ninham, The present state of affairs with Hofmeister effects, Curr. Opin. Colloid Interface Sci. **9**, 1 (2004).
[85] R. Tadmor, E. Hernández-Zapata, N. Chen, P. Pincus, and J. N. Israelachvili, Debye length and double-layer forces in polyelectrolyte solutions, Macromolecules **35**, 2380 (2002).
[86] W. Wang, K. Li, M. Ma, H. Jin, P. Angeli, and J. Gong, Review and perspectives of AFM application on the study of deformable drop/bubble interactions, Adv. Colloid Interface Sci. **225**, 88 (2015).